Small bodies of the solar system

Lecture by Klaus Jockers, Göttingen, winter term 2004/2005

- Why small bodies? Small bodies are “pristine”.
- Brief outline of our present understanding of solar system formation
- Small bodies: meteors and meteorites, *asteroids*, planetary satellites, *comets and Kuiper belt objects*
- Selection of topics depends to some extent on my research interest and is not exhaustive.
- Important textbook: Imke de Pater and Jack j. Lissauer: Planetary Sciences, Cambride Univ. Press 2001

Solar system formation

•Early stages (Ewine van Dieshoek, Leiden) a-d
•A lot of steps between d and e:
•Protoplanetary disk is hot near the Sun and cold far from the Sun, condensation of gas depending on temperature
• Formation and growth of planetesimals (strongly dependent on relative velocity)
• Formation of terrestrial and giant planets
• Early Jupiter prevents planetesimal growth in its neighborhood → origin of asteroids
• Comets originate in the Kuiper belt at about 40 AU from the Sun
•Long-period comets are scattered into Oort cloud, disturbed and isotropized by the influence of passing stars and the galactic bulge.
•Short-period comets go directly from Kuiper belt to the inner solar system
•Meteorites come from the surfaces of asteroids and from Mars to the Earth. Their measurement in the laboratory has contributed greatly to our knowledge about solar system formation.

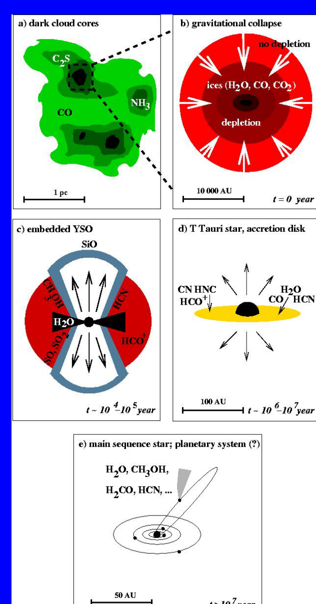

Asteroids

Orbits and their evolution

Ground-based observations

- Radiometry
- Photometric light curves
- Polarimetry of scattered light
- Radar
- Mass and density determination

Size distribution and collisional evolution

Surface composition, relation to meteorites, taxonomy
and spatial distribution of taxonomic classes

Surface structure from remote, disk-integrated observations

Images of the surface of asteroids with spaceborn cameras

Origin and evolution of the asteroid belt

Orbits and their evolution

Locations projected onto the ecliptic plane of approximately 7000 asteroids on 7 March 1997. The vast majority of the asteroids depicted are in the main asteroid belt, but Trojans are shown leading and trailing the position of Jupiter; Aten, Apollo and Amor asteroids are seen in the inner solar system, crossing the orbits of Mars and Earth.

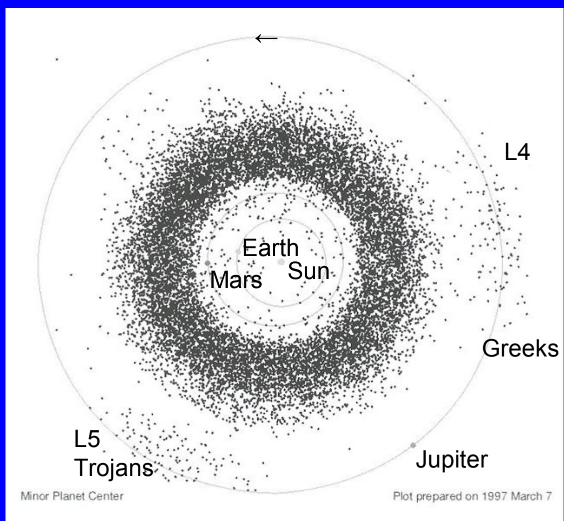

Orbital elements

- Time of perihelion passage T
- perihelion distance q
- excentricity e
- inclination i
- argument of perihelion ω
- node Ω

Osculating elements and their epoch
Periodic and secular perturbations

Orbital elements

672 J A Fernández and K Jockers

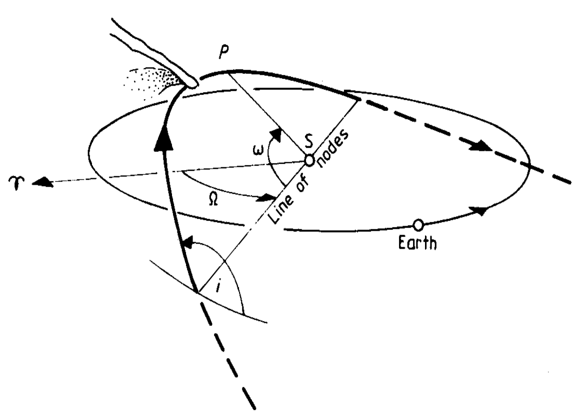

Figure 2. Main features of a comet moving on a typical very eccentric orbit. The symbols stand for: perihelion (P), inclination of the orbit with respect to the ecliptic plane (i), argument of perihelion (ω) and longitude of the ascending node (Ω) measured with reference to the vernal equinox (♈). Note that in this case the comet moves on a retrograde orbit with respect to the orbital motion of the Earth. Comet Halley moves on an orbit similar to the one represented here.

TABLE 9.1 Twenty Largest Asteroids (a < 6 AU).

#	Name	Diam. (km)	Tax. Class	a (AU)	e	i (deg)	Ω (deg)	ω (deg)	M (deg)	Period (yr)	Rotation (hr)
1	Ceres	933	G?	2.769	0.0780	10.61	80.0	71.2	287.3	4.607	9.075
2	Pallas	525		2.770	0.2347	34.81	172.6	309.8	273.8	4.611	7.811
4	Vesta	510	V	2.361	0.0906	7.14	103.4	150.1	43.3	3.629	5.342
10	Hygiea	429	C	3.138	0.1201	3.84	283.0	316.1	33.0	5.656	27.659
511	Davida	337	C	3.174	0.1784	15.94	107.3	339.0	244.5	5.656	5.130
704	Interamnia	333	F	3.064	0.1475	17.30	280.4	92.2	276.8	5.364	8.727
52	Europa	312	C	3.101	0.1002	7.44	128.6	337.0	92.6	5.460	5.631
15	Eunomia	272	S	2.644	0.1849	11.76	292.9	97.5	327.9	4.299	6.083
87	Sylvia	271	PC	3.490	0.0820	10.87	73.1	273.3	248.8	6.519	5.183
3	Juno	267	S	2.668	0.0258	13.00	169.9	246.7	115.4	4.359	7.210
16	Psyche	264	M	2.923	0.1335	3.09	149.9	227.5	318.7	4.999	4.196
31	Euphrosyne	248	C	3.146	0.2290	26.34	30.7	63.1	341.0	5.581	5.531
65	Cybele	240	C	3.437	0.1044	3.55	155.4	109.8	20.1	6.372	4.041
107	Camilla	237	C	3.484	0.0842	9.93	173.5	296.0	139.7	6.503	4.840
624	Hektor	233	D	5.181	0.0246	18.23	342.1	178.0	2.9	11.794	6.921
88	Thisbe	232	C	2.767	0.1638	5.22	276.3	35.3	259.0	4.603	6.042
451	Patientia	230	C	3.062	0.0709	15.24	89.0	343.2	269.4	5.358	9.727
324	Bamberga	228	C	2.681	0.3409	11.14	327.8	43.4	189.6	4.390	29.43
48	Doris	225	C	3.110	0.0693	6.54	183.4	262.8	278.8	5.485	11.89
532	Herculina	225	S	2.771	0.1764	16.36	107.4	75.1	199.4	4.613	9.405

All data are from Yoder (1995).

Imke de Pater and Jack j. Lissauer: Planetary Sciences, Cambride Univ. Press 2001

Histogram of all numbered asteroids brighter than 15th magnitude versus orbital period (with correspon-ding semi-major axes shown on the upper scale); the scale of the abscissa is logarithmic.

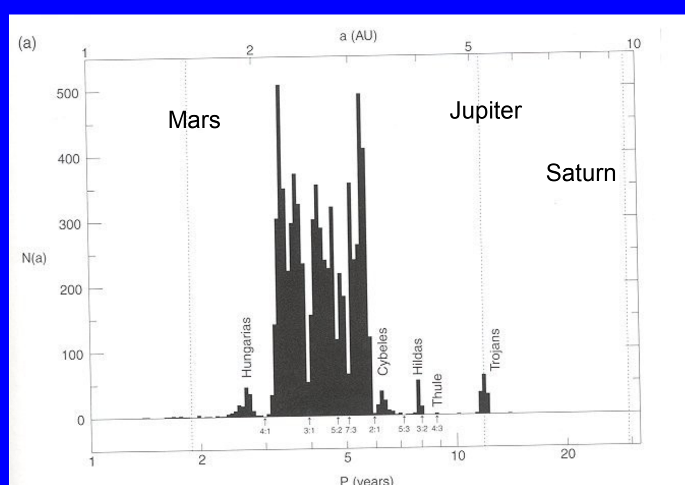

As asteroids with shorter optical periods are better lit and pass closer to Earth, there is a strong observational bias favoring objects plotted toward the left of the plot. Note the prominent gaps in the distribution for orbital periods ¼, ½, 3/7 and 1/3 that of Jupiter.

Stable resonance

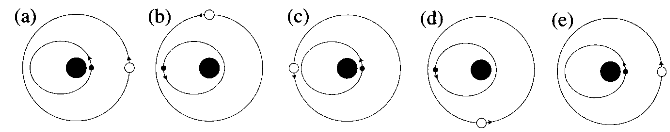

Fig. 8.1. The relative positions of Jupiter (white circle) and an asteroid (small filled circle) for the stable configuration when their orbital periods are in a ratio of 2:1. If T_J is the period of Jupiter's orbit then the diagrams illustrate the configurations at times (a) $t = 0$, (b) $t = \frac{1}{4}T_J$, (c) $t = \frac{1}{2}T_J$, (d) $t = \frac{3}{4}T_J$, and (e) $t = T_J$.

Unstable resonance

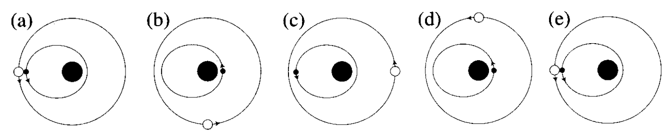

Fig. 8.2. The relative positions of Jupiter (white circle) and an asteroid (small filled circle) for the unstable configuration when their orbital periods are in a ratio of 2:1. If T_J is the period of Jupiter's orbit then the diagrams illustrate the configurations at times (a) $t = 0$, (b) $t = \frac{1}{4}T_J$, (c) $t = \frac{1}{2}T_J$, (d) $t = \frac{3}{4}T_J$, and (e) $t = T_J$.

Murray CD and Dermott SF, 1999: Solar system dynamics, Cambridge Univ. Press

Orbits and their evolution

- Main belt between 2.1 and 3.3 AU
- Kirkwood gaps coincide with resonance locations relative to Jupiter, which may be unstable or stable (Hildas, Thule)
- At inner edge of asteroid belt ν_6 resonance with Saturn's apse rate
- ~700 asteroids occupy L_4 and L_5 triangular Lagrange points → Trojans (separated into Trojans and Greeks)
- Trojans, 4/3 and 3/2 librators and main belt asteroids occupy the only known stable orbits in Solar System
- Unstable orbits: Amors (1.017<q<1.3), Apollos (q < 1.017, a > 1) and Atens (a < 1), all small objects
- Centaurs: 944 Hidalgo (a=5.8 au), 2060 Chiron (a=13.7 au, may be comet), 1994 TA (a=17.5 au), 5145 Pholus (a=13.7 au), 7066 Nessus (a=24.9 au), chaotic orbits
- Kuiper belt objects (see later)

The „outburst“ of 2060 Chiron; a graph of the magnitude of Chiron as a function of time, which clearly shows Chiron‘s dramatic increase in brightness starting in 1987. The data were taken by different groups, as symbolized by the different symbols used. (Lazzaro et al. 1997)

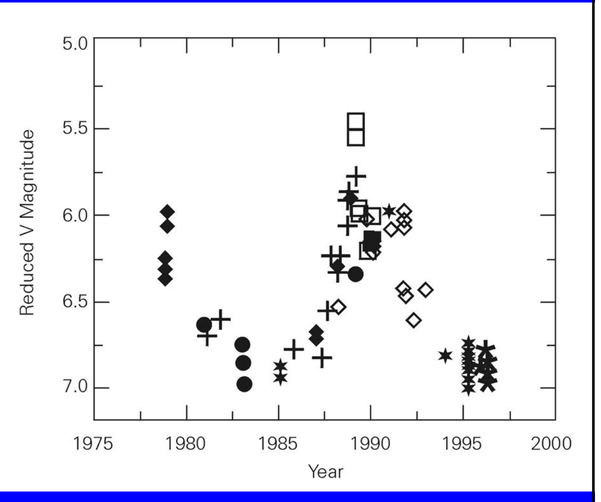

Coordinates of asteroids in a-i space

Families are indicative of collisional processes between asteroids.

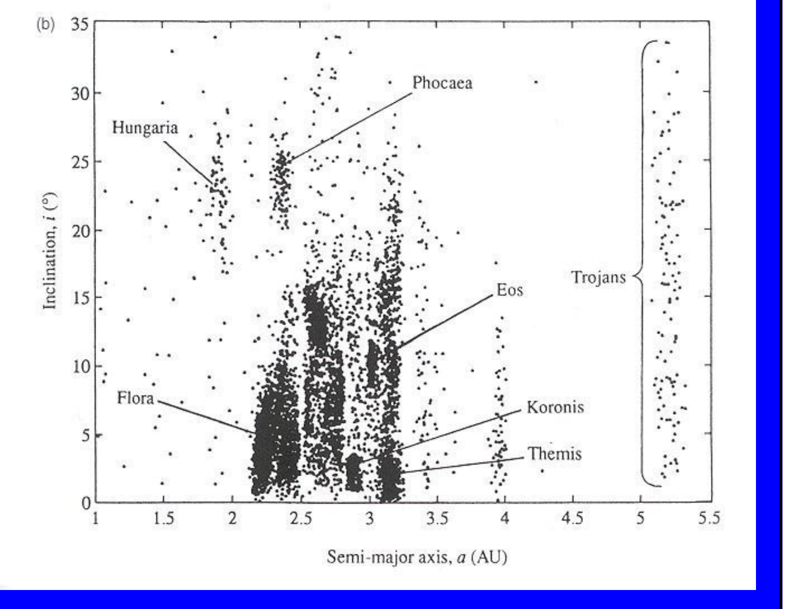

Asteroids, Ground-based Observations

We want to know the physical nature of asteroids.

•Remote sensing of asteroids in the visual and infrared range allows us to determine the size of the asteroids via an albedo determination.
•The albedo can also be determined from polarimetric measurements.
•Besides of this, photometric and polarimetric phase curves contain information on surface texture and regolith properties, but interpretation of these phase curves is still a matter of debate.
•Radar studies of asteroids are very interesting but at present are limited to objects which approach the Earth closely.

Radiation laws related to Planck's law

$$B_\nu(T)d\nu = \frac{2h\nu^3}{c^2}\frac{1}{e^{h\nu/kT}-1}d\nu \quad \text{W m}^{-2}\text{ rad}^{-2}$$

or, using

$$B_\lambda(T)d\lambda = B_\nu(T)d\lambda \cdot c/\lambda^2$$

$$B_\lambda(T)d\lambda = \frac{2hc^2}{\lambda^5}\frac{1}{e^{hc/\lambda kT}-1}d\lambda \quad \text{W m}^{-2}\text{ rad}^{-2}$$

$$\frac{h\nu}{kT} \gg 1 \qquad B_\nu(T) \approx \frac{2h\nu^3}{c^2}e^{-h\nu/kT}d\nu \qquad \text{Wien}$$

$$\frac{h\nu}{kT} \ll 1 \qquad B_\nu(T) \approx \frac{2\nu^2 kT}{c^2} \qquad \text{Rayleigh-Jeans}$$

Wien's displacement law:

$$\frac{c}{\nu_{max}} \cdot T = 5.10 \cdot 10^{-3} \quad \text{[meter K]} \qquad \text{or}$$

$$\lambda_{max} \cdot T = 2.90 \cdot 10^{-3} \quad \text{[meter K]}$$

With T = 290 K (room temperature) we get $\lambda_{max} = 10^{-5}$ m = $10\ \mu$m.
With T = 5800 K (solar-type star) we get $\lambda_{max} = 0.5\ \mu$m.

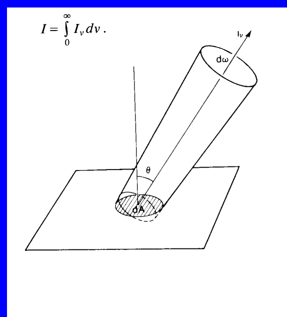

Figure from Karttunen et al. Fundamental Astronomy, Springer 1987, p. 87

Stefan-Boltzmann law and mean temperature of a solar system body

Isotropic emission by a blackbody:

$$F_\nu = \int_S I_\nu \cos\theta \, d\omega \quad I \text{ intensity [W m}^{-2}\text{ rad}^{-2}]$$

ω denotes solid angle and θ colatitude.
If the body radiates isotropically,

$$F_\nu = I_\nu \int_S \cos\theta \, d\phi \, sin\theta \, d\theta = \pi I_\nu.$$

Likewise, for a blackbody

$$F = \pi \int_0^\infty B_\nu(T) d\nu = \sigma T^4 \quad \text{W m}^{-2}$$

with $\sigma = \frac{2\pi^5 k^4}{15 c^2 h^3} = 5.67 \cdot 10^{-8}$ W m^{-2} T^{-4}

A solar system body is irradiated by the Sun:

$$\frac{1}{4}(1 - A_{VIS})\frac{F_\odot}{r^2} = (1 - A_{IR})\sigma T^4$$

$F_\odot = 1.360 \cdot 10^3$ W m^{-2} is the solar constant at 1 au. r is the heliocentric distance in au. For a black body albedo $A_{VIS} = A_{IR} = 0$. The equation assumes isotropic thermal emission (not quite true!).

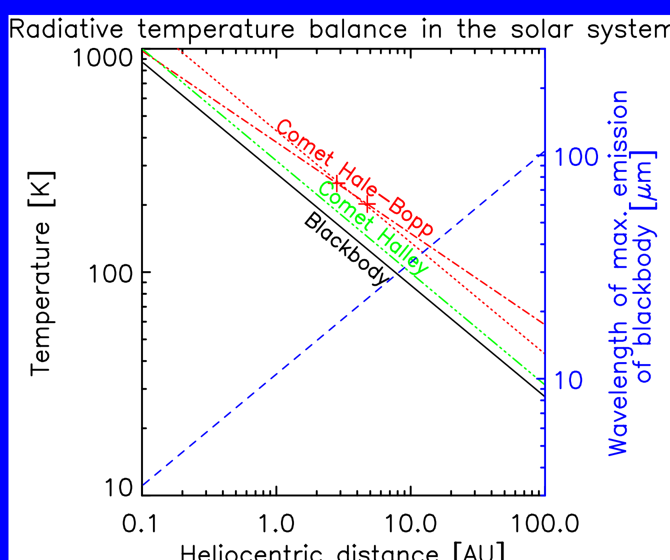

Observations of cometary dust in the visual and infrared wavelength range.

From:
Gehrz and Ney:
0.7 µm to 23 µm photometric observations of P/Halley and 6 recent bright comets, Icarus 100, 162-186, 1992

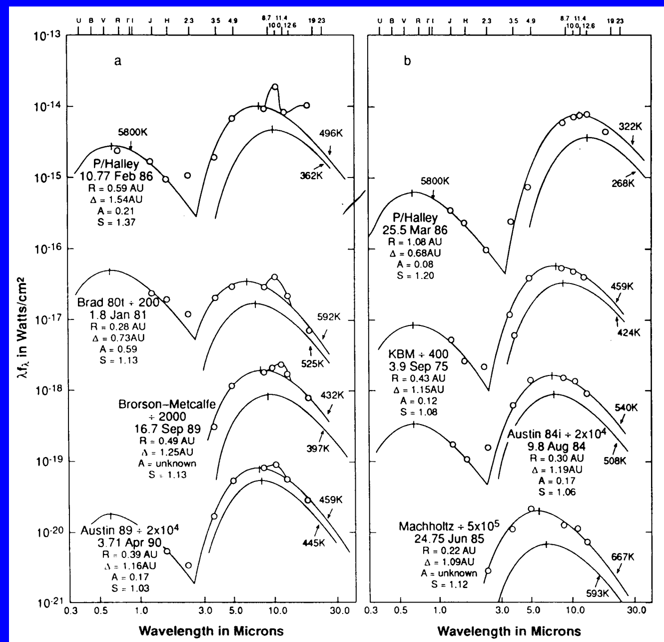

From: Morrison and Lebovsky, Gehrels ed. Asteroids, U. Ariz. Press, 1979

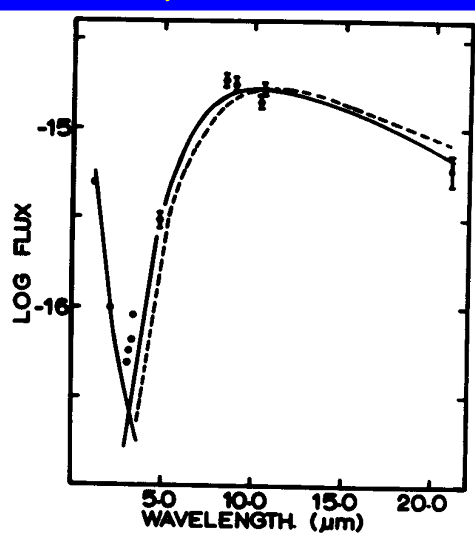

Fig. 1. The observed flux of 324 Bamberga from 1.25–21 μm. A solar spectrum has been fit through the K-band measurement and a least squares fit has been made to the thermal infrared measurements (5–21 μm). Solid line: dusty model. Dashed line: rocky model.

Albedos and phase function 1

α = Phase angle, $\theta = 180^0 - \alpha$ = scattering angle, ε = (solar) elongation

Imke de Pater and Jack j. Lissauer: Planetary Sciences, Cambride Univ. Press 2001 ↓

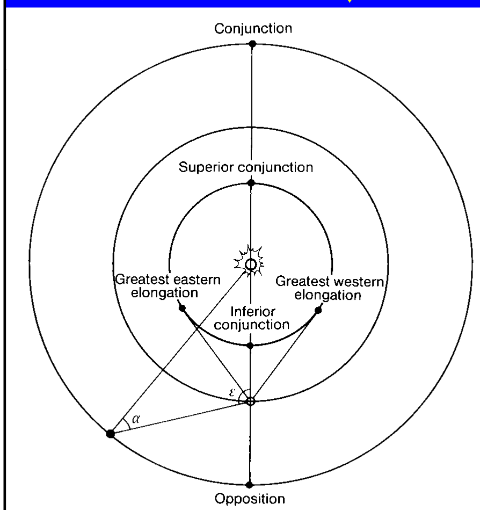

Куликовский ПГ, Справочник любителя астрономии, Moscow 1971↓

To Sun
↑

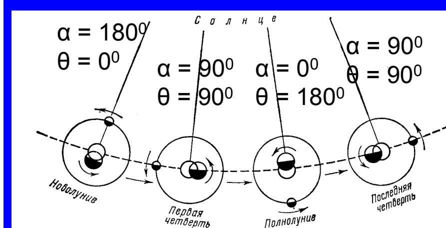

Рис. 12. Движение Земли и Луны вокруг барицентра и фазы Луны.

Albedos and phase function 2

Definition of albedos (Karttunen et al, Fundamental Astronomy, Springer 1987)

Bolometric albedo A: ratio of the total emergent flux to the total incident flux

Bond albedo A_ν: ratio of the emergent flux to the incident flux *for a fixed frequency*

Phase function: $\Phi(\alpha)$: angular dependence of emergent radiation, $\Phi(\alpha = 0) = 1$.

Phase integral: $q = 2 \cdot \int_0^\pi \Phi(\alpha) \sin\alpha \, d\alpha.$

Lambertian surface: absolutely white, diffuse surface, which reflects all radiation (i.e. $A = 1$ or $A_\nu = 1$). It has phase function $\Phi(\alpha) = \cos\alpha$ for $0 \le \alpha \le \pi/2$ and $\Phi(\alpha) = 0$ for $\pi/2 < \alpha < \pi$.

Geometric albedo p: The geometric albedo is the ratio of the flux densities at phase angle $\alpha = 0$, reflected by a planet and by a Lambertian surface.

$$p = A/(2\int_0^\pi \Phi(\alpha) \sin\alpha \, d\alpha) = A/q.$$

For isotropic emission $\Phi(\alpha) \equiv 1$, $q = 4$ and $p = A/4$
(note: for a sphere 4 = surface area / cross-section area).

For a Lambertian surface $q = 2\int_0^{\pi/2} \cos\alpha \sin\alpha \, d\alpha = 1$ and $p = 1$.

Albedos and phase function 3

Planetary photometry (Karttunen et al, Fundamental Astronomy, Springer 1987)

Flux from a planet: $F_p = \frac{p\,\Phi(\alpha)}{\pi}\frac{F_\odot}{\Delta^2\ r^2}\pi R^2.$

F_p flux from the planet, p geometric albedo, $\Phi(\alpha)$ phase function, Δ geocentric distance of planet, $F_\odot$ solar flux at Earth (solar constant), R planetary radius. All lengths are measured in astronomical units (au).

In terms of stellar magnitudes:
$$\begin{aligned} m_p - m_\odot &= -2.5\lg\frac{F_p}{F_\odot} = -2.5\lg\frac{p\Phi(\alpha)R^2}{\Delta^2 r^2} \\ &= -2.5\lg pR^2 + 5\lg r\Delta - 2.5\lg\Phi(\alpha). \end{aligned}$$

We now define the absolute magnitude: $V(1,0) = m_\odot + 5\lg r\Delta - 2.5\lg\Phi(\alpha).$

V(1,0) is the magnitude of a body if it is at a distance of 1 au from Earth and Sun at phase angle $\alpha = 0$.

Then the magnitude of a planet can be expressed as $m_p = V(1,0) + 5\lg r\Delta - 2.5 lg\Phi(\alpha).$

Thermal models of asteroids

$$\pi R^2(1 - A_{VIS})\frac{F_\odot}{r^2} = \beta\epsilon\sigma R^2\int_0^{2\pi}\int_{-\pi/2}^{\pi/2} T^4(\theta,\phi)\cos\phi\, d\phi d\theta$$

ϵ is the bolometric emissivity, σ the Boltzmann constant, β is a normalization constant (of order unity related to the angular distribution of thermal emission).

An important consideration is the thermal inertia of the asteroidal surface. For low thermal inertia (like on the moon) one can assume:

$$T = T_{max}\cos^{\frac{1}{4}}\theta\ \cos^{\frac{1}{4}}\phi$$

Using this formalism one can determine the albedo A_{vis} and from this the diameter of the asteroid. But thermal models of asteroids are also interesting by themselves as they allow to study the asteroid regolith.

Irradiation of an asteroid by the Sun

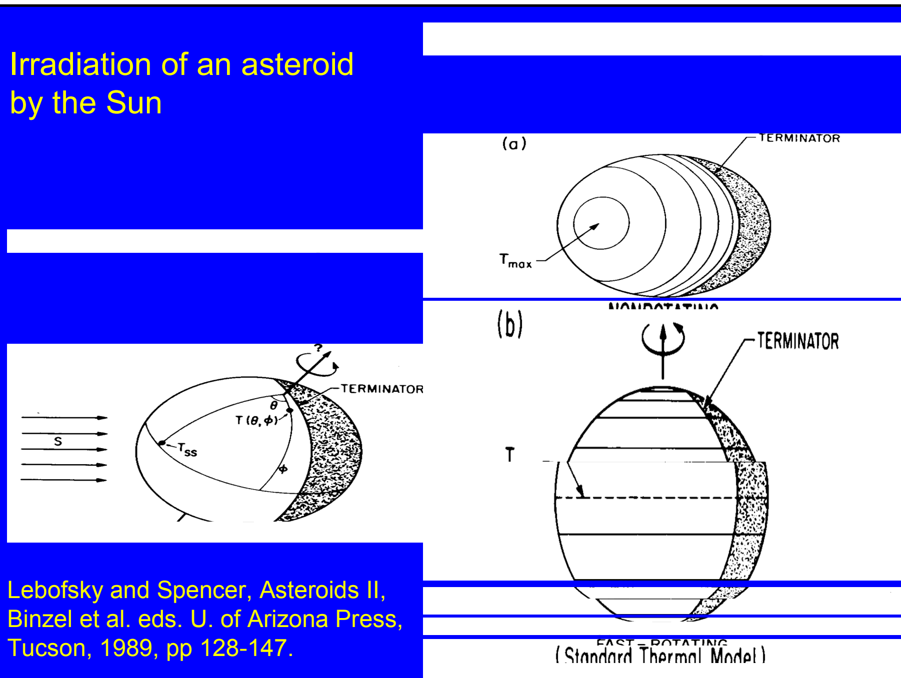

Lebofsky and Spencer, Asteroids II, Binzel et al. eds. U. of Arizona Press, Tucson, 1989, pp 128-147.

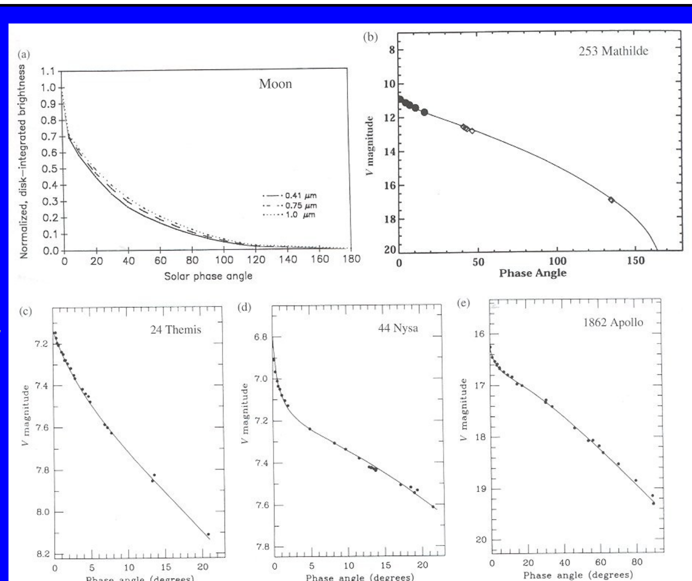

(a) Brightness of the Moon as function of solar phase angle, at three different wavelengths. The data at small phase angles (< 5°) were derived from Clementine data. (Buratti *et al.* 1996) (b) Phase function of 253 Mathilde, as determined from ground based (filled circles) and NEAR whole-disk 0.70 μm data (diamonds) (Clark *et al.* 1998). Asteroid magnitude as a function of phase angle for 24 Themis (c), 44 Nysa (d) and 1862 Apollo (e). Note the anomalous increase in intensity near Φ = 0° (Bowell *et al.* 1989). The data are compared to best-fit Hapke models.

Remember: Phase integral q = 1 for the Lambertian surface.

TABLE 9.2 Albedos and Phase Functions for Various Airless Bodies.

Body	$A_{0,v}$	$q_{ph,v}$	A_v	A_b	Ref.
Moon	0.113	0.611	0.069	0.123	1
Mercury	0.138	0.486	0.067	0.119	1
243 Ida	0.21	0.34	0.071	0.081	2
Dactyl	0.20	0.32	0.064	0.073	2
253 Mathilde	0.047	0.280	0.013		3
433 Eros	0.29	0.39	0.11	0.12	4
951 Gaspra	0.23	0.47	0.11		5
Phobos	0.071	0.300	0.021		6
Deimos	0.068	0.390	0.027		7

1: Veverka *et al.* (1988). 2: Veverka *et al.* (1996). 3: Clark *et al.* (1999). 4: Domingue *et al.* (2001). 5: Helfenstein *et al.* (1994). 6: Simonelli *et al.* (1998). 7: Thomas *et al.* (1996).

The plane Sun-Object-Observer we have already dealt with is the plane of light scattering of the radiating reaching us from the Sun via the planet. It is a symmetry-breaking plane, and, because of this, makes the light from the planet polarized (from Karttunen et al., Fundamental Astronomy).

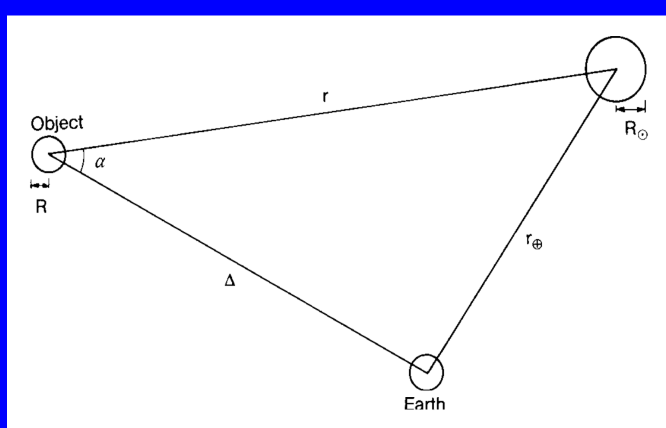

Opposition peak: shadow hiding versus coherent backscattering

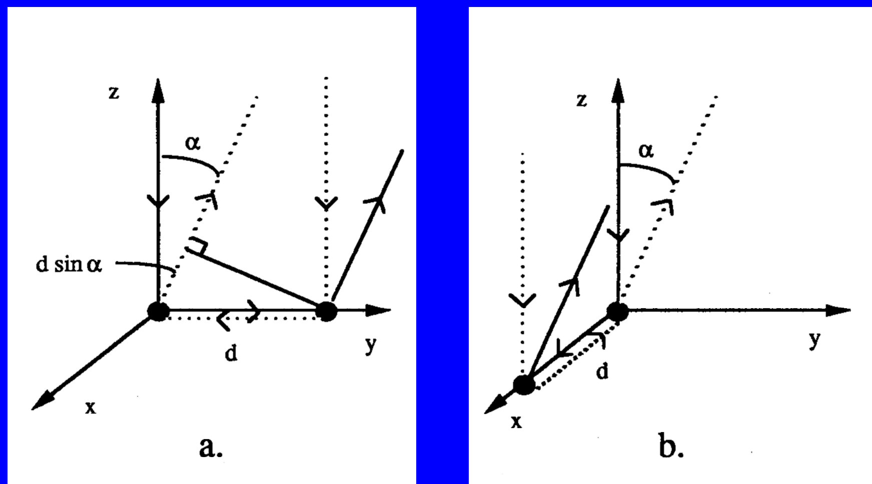

Coherent mechanism of backscattering: Muinonen K. Abstract of thesis, Helsinki 1990

Brightness peak at zero phase angle is accompanied by a negative branch of ("anomalous") polarization, as predicted by the model of coherent backscattering.

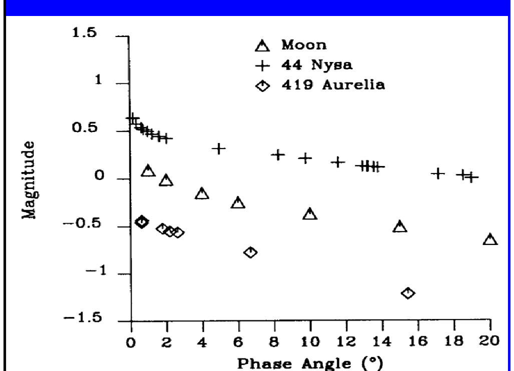

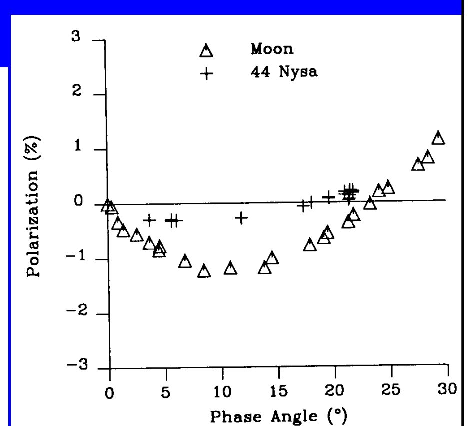

(a) Degree of linear polarization as a function of solar phase angle F for asteroid 1 Ceres. Definitions for the various polarization parameters are shown. (Dollfus *et al.* 1989).

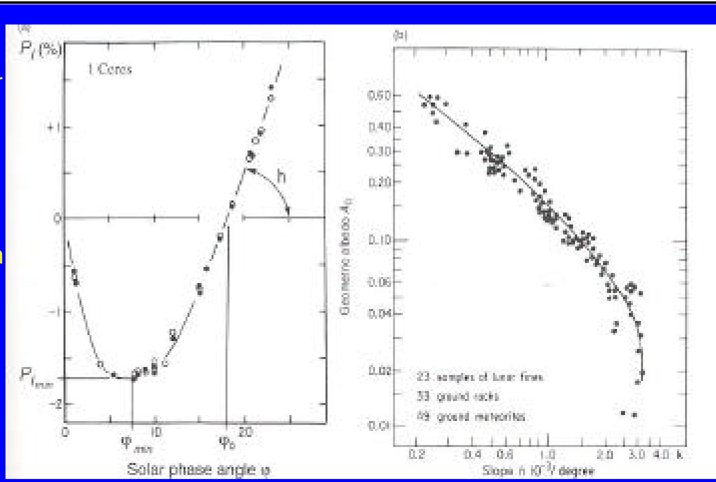

(b) The relationship between the slope, *h* (see panel (a)), and the albedo $A_{0,\ F=5°}$, normalized to the case of a white magnesium oxide surface. (Dollfus *et al.* 1989).

Imke de Pater and Jack j. Lissauer: Planetary Sciences, Cambride Univ. Press 2001

Kiselev, private communi-cation

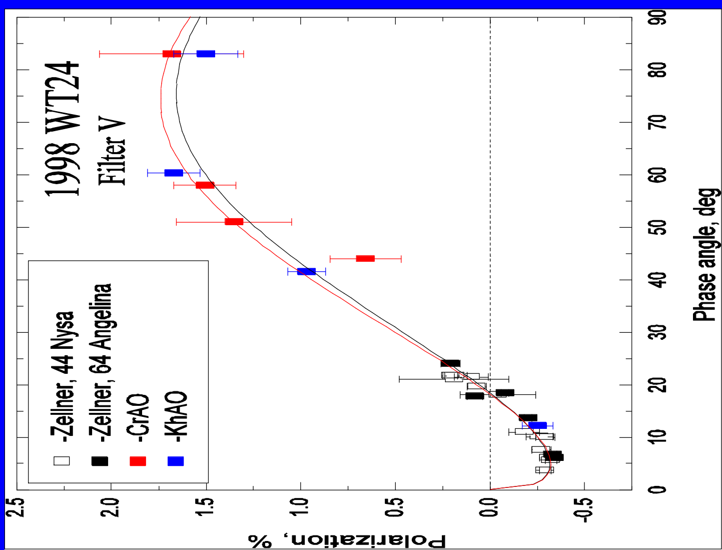

1998 WT24, a small near Earth asteroid of E-type

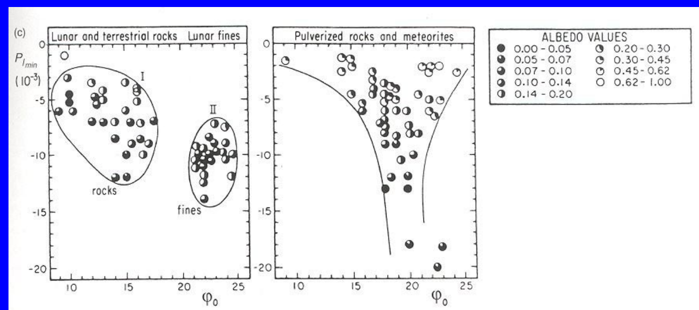

(c) A graph of P_{Lmin} versus φ_0 for: left, lunar and terrestrial rocks (region I) and rock powders and lunar fines (region II); right , meteorites and rocks with grain sizes between 30 and 300 µm lie in between these two regions. (Dollfus *et al.* 1989)

Dependences of α_{inv} and P_{min} on average particle diameter measured in laboratory experiments. Filled circles, crosses, and open circles correspond to green, clear, and black glass, respectively (after Shkuratov et al. Earth, Moon, and Planets 1994, 65, 201-246).

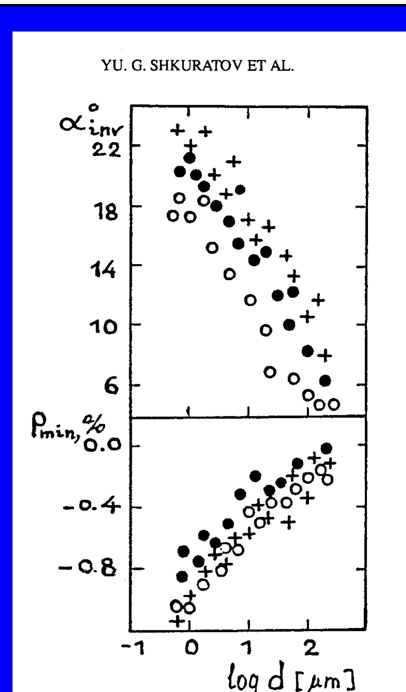

232 YU. G. SHKURATOV ET AL.

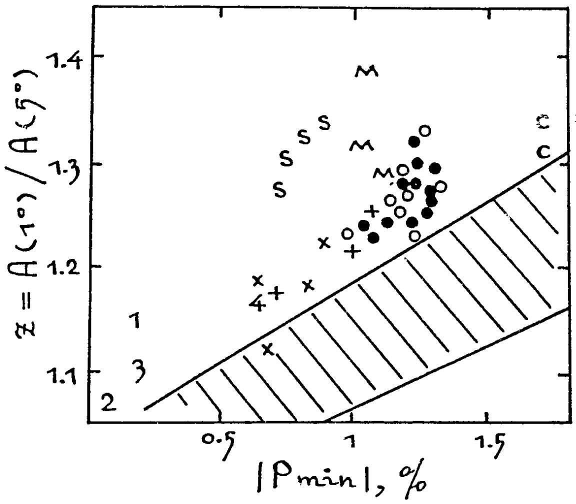

Fig. 25. The relationship between negative polarization and opposition-effect parameters. The shaded domain contains laboratory measurements by Shkuratov *et al.* (1989), filled circles pertain to lunar maria, open circles to lunar highlands, crosses to lunar highland craters, pluses to lunar mare craters, and the symbols *C*, *S*, and *M* to the corresponding asteroid taxa.

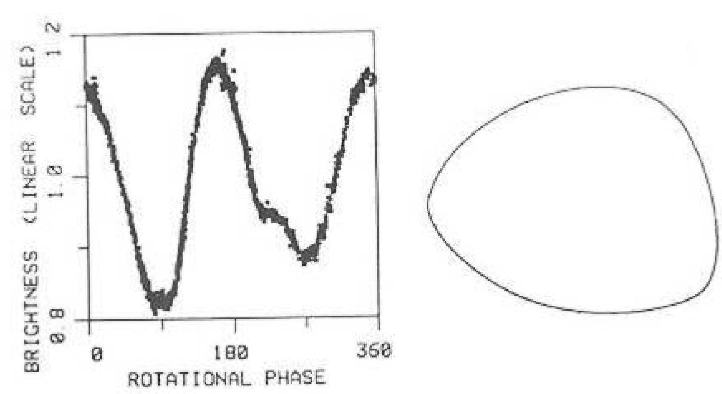

Photometric lightcurve of the asteroid 164 Eva. The lightcurve is shown on the left. The curve can be matched by the solid profile on the right; imagine this as a two-dimensional, geometrically scattering asteroid. As this asteroid rotates, it generates a lightcurve similar to that shown on the left. (Magnusson *et al.*, Asteroids II, Binzel et al. eds., U. of Arizona Press, pp.66-97. 1989)

Radar echo spectrum of near-Earth asteroid 1620 Geographos obtained in 1994 at Goldstone at a transmitter frequency of 8510 MHz. The echo power is plotted in standard deviations versus Doppler frequency (in Hz) relative to the estimated fre-quency of echoes from the asteroid's center-of –mass.

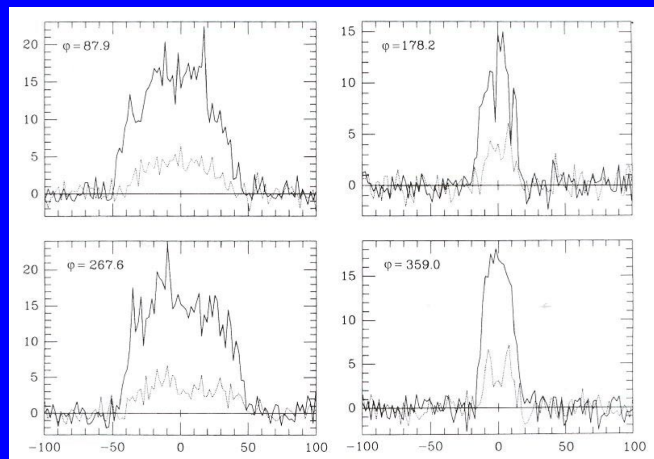

Objects may be irregular on scales exceeding meters, yet smooth on centimeter scales.

Solid and dotted lines are echoes in the *OC* and *SC* polarizations, respectively. These spectra are at rotational phases, φ, which correspond to bandwidth extrema. (Ostro *et al.* 1996, Icarus 121, 44-66)

A cartoon on the geometric relationship between echo power and an asteroid's shape. The upper picture shows the convex hull *H* of the polar silhouette, or the asteroid shape as viewed from the pole. The middle panel shows a view along the radar line of sight, and the radar echo is shown at the bottom. The plane ψ_0 contains the line of sight and the asteroid's spin vector. The radar echo from any part of the asteroid which intersects ψ_0 has a Doppler frequency ν_0. The cross-hatched strip of power in the spectrum corresponds to echoes from the cross-hatched strip on the asteroid. The asteroid's polar silhouette can be estimated from echo spectra which are adequately distributed in rotational phase. (Ostro 1989, see Imke de Pater and Jack j. Lissauer: Planetary Sciences)

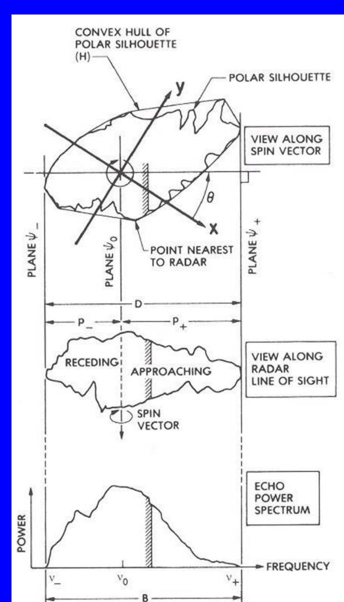

Radar “images”:
a: 4179 Toutatis
b: 1620 Geographos
c: 4769 Castalia
d: 216 Kleopatra

From Ostro et al. 1995, 1996, 2000, Hudson and Ostro 1994, see Imke de Pater and Jack j. Lissauer: Planetary Sciences, Cambride Univ. Press 2001

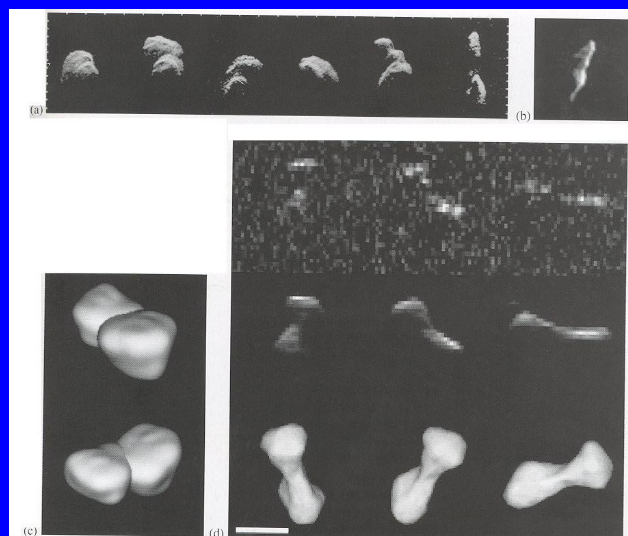

Radio images of 324 Bamberga at 8510 MHz, obtained with a bistatic radar system where the Goldstone antenna was used to transmit the signal and the VLA to receive and image the radar echo. Radar echoes are shown for 13 September 1991, in the center channel (solid contours), and channels at a Doppler frequency of -381 Hz (dashed contours; redshifted) and +381 Hz (dot-dashed contours; blueshifted). Contour levels are from 3 to 19 standard deviations, where one standard deviation is 5.5 mJy/beam.

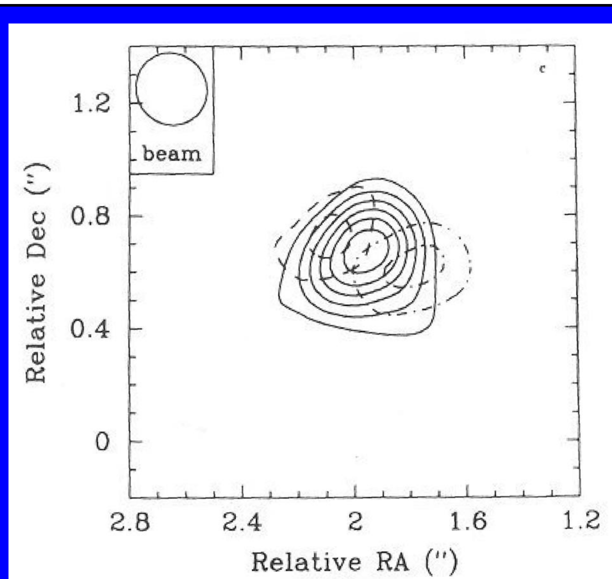

Imke de Pater and Jack j. Lissauer: Planetary Sciences, Cambride Univ. Press 2001

More on opposition effect:
Scattering properties of planetary regoliths near opposition:
Y. Shkuratov, G. Videen M.Kreslavsky, I. Belskaya, V. Kaydash, A. Ovcharenko, V. Omelchenko, N. Opanasenko, E. Zubko, in:
G. Videen, Y. Yatskiv and M. Mishchenko eds.: Photopolarimetry in Remote sensing, NATO Science Series Vol. 161, Kluwer 2004, 191-208

Opposition spot, photographed from airplane over the Arizona desert.

Albedo image (left) and phase ratio image (right) of a portion of Sinus Medii on the moon

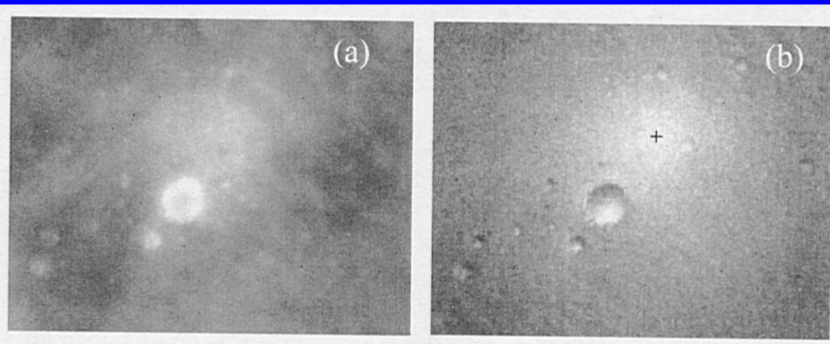

Figure 3. (a) An albedo image of a portion of Sinus Medii acquired at near zero phase angle. The brightness opposition surge cannot be distinguished from the albedo variation. (b) A phase-ratio image for the same site makes the surge clearly visible. The center of the surge (zero-phase angle point) is denoted with the black cross.

Moon, brightness and polarization phase curves

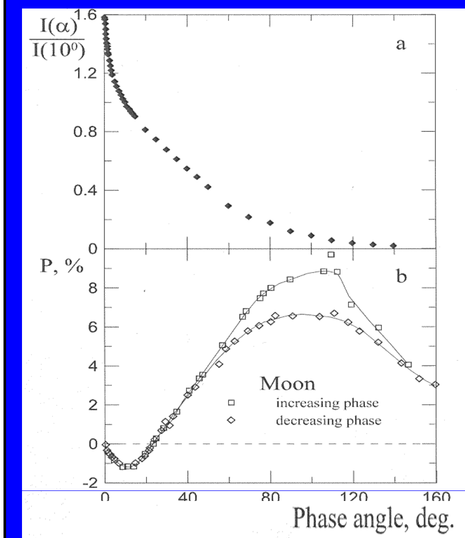

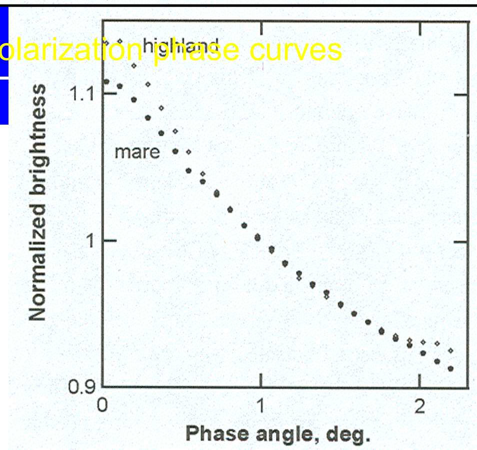

curves of brightness of the lunar mare and highlands at 1 μm [31].

Figure 7. Albedo (a) and $|P_{min}|$ (b) images of the lunar nearside [39]. Darker shades in the right panel correspond to lower values of $|P_{min}|$.

Note: $|P_{min}|$ (right side) is blacker when the phase curve of polarization is shallower, i.e. this is part of Umov's law (higher albedo means smaller polarization)

The jovian moon Europa as an example of a very high albedo icy object

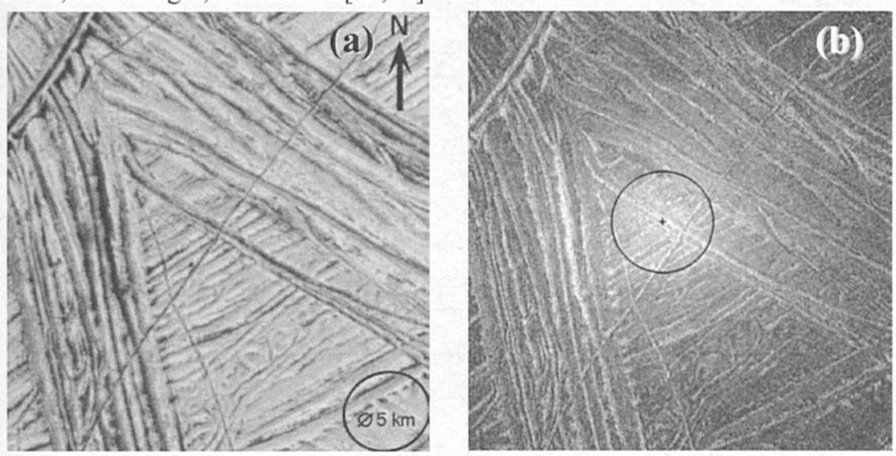

Figure 10. Albedo (a) and phase-ratio $I(\sim 0°)/I(3°)$ (b) images of Europa's surface obtained with the Galileo camera using a 0.56 µm filter [33].

Anomalous (coherent) polarization with two minima.
Lycopodium spores: uniform particles, diam. ≈ 20µm, fairly bight, not transparent, roundish.

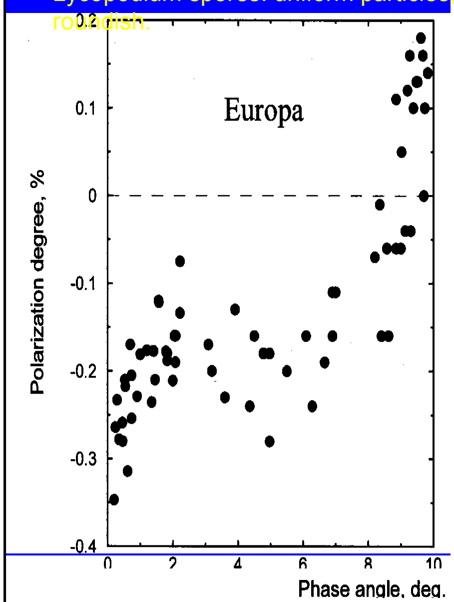

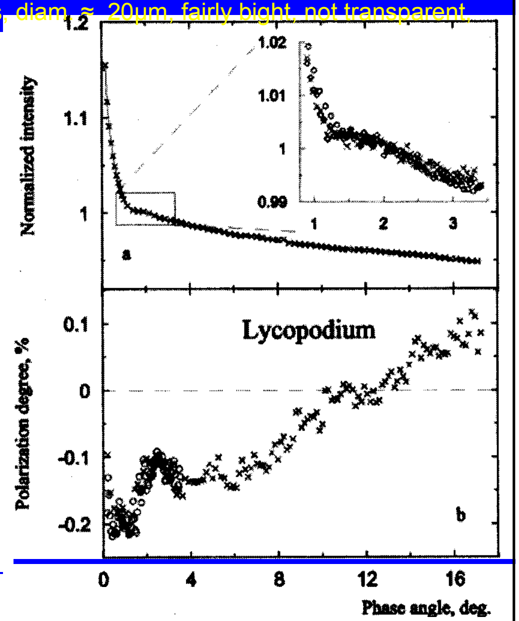

Close-ups of asteroids

Note:
Irregular shape,
cratering,
regolith